Mechanically stimulated osteocytes maintain tumor dormancy in bone metastasis of non-small cell lung cancer by releasing small extracellular vesicles

Jing Xie[1,2,5], Yafei Xu[1,5], Xuhua Liu[4], Li Long[2], Ji Chen[2], Yan Shao[4], Zhiqing Cai[2], Zhimin Zhang[2], Ruixin Zhou[2], Jiarong Leng[3], Xiaochun Bai[2]✉ and Qiancheng Song[2, 3]✉

[1]General Practice Centre, The Seventh Affiliated Hospital, Southern Medical University, Foshan, Guangdong, 528000, China.

[2]Guangdong Provincial Key Laboratory of Bone and Joint Degeneration Diseases, Department of Cell Biology, School of Basic Medical Sciences, Southern Medical University, Guangzhou, 510515, China.

[3]Department of Neurosurgery, Institute of Brain Diseases, Nanfang Hospital of Southern Medical University, Guangzhou, 510515, China.

[4]Academy of Orthopedics, Guangdong Province, Guangdong Provincial Key Laboratory of Bone and Joint Degeneration Diseases, The Third Affiliated Hospital of Southern Medical University, Guangzhou, 510630, China.

[5]These authors contributed equally: Jing Xie, Yafei Xu.

✉email: baixc15@smu.edu.cn; songqc@smu.edu.cn

Abstract

Although preclinical and clinical studies have shown that exercise can inhibit bone metastasis progression, the mechanism remains poorly understood. Here, we found that non-small cell lung cancer (NSCLC) cells adjacent to bone tissue had a much lower proliferative capacity than the surrounding tumor cells. Subsequently, it was demonstrated that osteocytes, sensing mechanical stimulation generated by exercise, inhibit NSCLC cell proliferation and sustain the dormancy thereof by releasing small extracellular vesicles with tumor suppressor micro RNAs, such as miR-99b-3p. Furthermore, mechanical loading of the tibia inhibited the bone metastasis progression of NSCLC. Notably, bone metastasis progression of NSCLC was inhibited by moderate exercise, and combinations with zoledronic acid had additive effects. Moreover, exercise preconditioning effectively suppressed bone metastasis progression. This study significantly advances the understanding of the mechanism underlying exercise-afforded protection against bone metastasis progression.

32 **Introduction**

33 Lung cancer is the second most common cancer type and the leading global cause of cancer
34 mortality (18.0% of the total cancer deaths) [1]. Approximately 85% of lung cancer patients have a
35 group of histological subtypes collectively termed non-small cell lung cancer (NSCLC) [2]. Despite
36 important advancements in NSCLC treatment that have been achieved over the past two decades,
37 prognosis remains poor owing to the presence of locally advanced or widely metastatic tumors in
38 most patients at the time of diagnosis [2]. Approximately 20% – 30% of patients with NSCLC
39 present with bone metastases at diagnosis, and 35% – 60% will develop them during their disease
40 course [3,4]. Bone metastases are frequent events associated with advanced-stage malignancies and
41 often cause skeletal-related events (SREs) such as severe bone pain, pathological fractures, spinal
42 cord compression, and hypercalcemia, which reduce the quality of life and predict a poor
43 prognosis [3,5,6]. In general, bone metastases are incurable; goals of management include
44 maximizing symptom control, preserving function, minimizing SREs, and enhancing local tumor
45 control [2,7]. A multi-disciplinary treatment approach is required, including pain management,
46 osteoclast inhibitors and other bone-specific therapy, systemic anti-cancer therapy, surgery,
47 radiation, and interventional techniques. Although there have been many advances in treatment,
48 the median survival from diagnosis of bone metastases has been reported to be very short in
49 patients with lung cancer [2,7]. Therefore, it is of considerable clinical significance to elucidate the
50 mechanism of bone metastasis and to find new drugs and combination therapies for bone
51 metastasis prevention and treatment in NSCLC.

52 Many preclinical and clinical studies have shown that exercise can reduce the incidence of
53 various cancers, inhibit cancer progression, reduce symptom burden, mitigate side effects of

54 cancer treatment, and improve survival and the quality of life in patients with cancer [8-11]. In
55 contrast, sedentary behavior and lack of physical activity is positively associated with an increased
56 risk for cancer and mortality [12,13]. Exercise is safe perioperatively, and multiple international
57 organizations have published exercise recommendations for patients with cancer [10,11,14]. The
58 evidence to-date suggests a benefit of exercise in all stages of lung cancer and lung cancer
59 survivors [10]. Exercise has the potential to improve physical function and the quality of life in
60 individuals with bone metastases and appears safe and feasible when it includes an element of
61 supervised exercise instruction [11,15]. The optimal exercise prescription for patients with bone
62 metastases is currently undefined [14,16]. Each patient with cancer may require a more personalized
63 exercise prescription. Therefore, a clearer understanding of the mechanisms by which exercise
64 modulates tumors is required.

65 Exercise induces systemic changes involving every system over the entire body, including
66 circulating substances, the immune system, and metabolism [17-19]. Throughout life, the skeleton
67 undergoes continuous remodeling, which is a balance between the resorption of mineralized bone
68 by bone-resorbing cells (osteoclasts) and new bone formation by bone-forming cells (osteoblasts)
69 [20]. Osteocytes, the most abundant cell type in bone, are terminally differentiated osteoblasts that
70 have become buried in their own matrix. During this process, their morphology changes to stellate,
71 facilitating the formation of an extensive interconnected network throughout the bone matrix
72 termed the lacunar-canalicular network (LCN) [21-23]. Through the LCN, osteocytes sense
73 mechanical stimulus and translate them into biochemical signals, and appropriately control bone
74 homeostasis by regulating the function of both osteoclasts and osteoblasts. Therefore, the

75 osteocyte is now recognized as a major orchestrator of the bone remodeling process. However, the
76 understanding of the relationship between osteocytes and bone metastasis remains limited.

77 Bone metastasis is a multistage process. Long before the development of clinically detectable
78 metastases, circulating tumor cells settle and enter a dormant state in normal vascular and
79 endosteal niches present in the bone marrow, which provide immediate attachment and shelter,
80 and the cells only become active years later as they proliferate and alter the functions of
81 osteoclasts and osteoblasts, promoting skeletal destruction [24]. The endosteal niche, including
82 osteoblasts and osteoclasts, has been reported to provide tumor cells with an environment
83 supporting their survival and outgrowth, however, the role of osteocytes has been rarely addressed
84 [5]. Tumor cell dormancy is defined as an arrest in the cell cycle [25,26]. The details of niches and
85 signals that support tumor cell dormancy in bone metastasis are largely unknown. In the current
86 study, we discuss the effect of exercise on bone metastasis of NSCLC, and investigated the
87 potential effects and mechanisms of the osteocyte on the dormancy of bone metastasis NSCLC
88 cells.

89

90 ## Results

91 **Osteocytes inhibited NSCLC cell proliferation.**

92 To study the spatial distribution of NSCLC cell proliferation in bone metastasis, bone metastasis
93 tissues of six NSCLC patients were obtained. Bone destruction was found in the presence of bone
94 metastasis in NSCLC (Supplemental Figure 1a). Surprisingly, immunohistochemical staining
95 showed that Ki-67 was much lower in tumor cells adjacent to bone tissue than in the surrounding
96 tumor cells (Figure 1a). An intraosseous model was used to investigate the biological progression

97 of NSCLC cells in a bone microenvironment via direct tibial implantation of A549 in nude mice.
98 The results of biophotonic imaging, micro-CT, and hematoxylin and eosin (H&E) staining
99 indicated that the model was successfully established 21 days after modeling (Supplemental
100 Figure 1, b – d). Consistent with the result in the clinical samples, Ki-67 expression was much
101 lower in tumor cells adjacent to bone tissue than in the surrounding tumor cells (Figure 1b). The
102 above results indicated that NSCLC cells adjacent to bone tissue have a much lower proliferative
103 capacity than the surrounding tumor cells. Therefore, we hypothesized that bone tissues release
104 some substance that inhibits tumor growth.
105 To determine which type of cell inhibits proliferation after NSCLC cells have invaded bone
106 tissue, A549 was co-cultured with MLO-Y4 and MC3T3-E1 for 48 h, respectively (Figure 1c).
107 We found that the A549 migration ability was improved after co-culture with MLO-Y4, with the
108 promotional effect being much significantly stronger on co-culture with MC3T3-E1
109 (Supplemental Figure 1e). More importantly, NSCLC cell proliferation was inhibited after
110 co-culture with MLO-Y4, whereas no inhibitory effect was found after co-culture with MC3T3-E1
111 (Figure 1d, e and Supplemental Figure 1f), indicating that it is osteocytes that inhibit NSCLC cell
112 proliferation. Surprisingly, MC3T3-E1 proliferation was effectively enhanced on co-culture with
113 MLO-Y4 (Figure 1f), which indicated that the effect of osteocytes on NSCLC cell and osteoblast
114 proliferation were different. Taken together, these data suggested that it is osteocytes that inhibit
115 NSCLC cell proliferation in the endosteal niche.
116 **Osteocyte small extracellular vesicles inhibited NSCLC cell proliferation.**
117 To investigate the mechanism by which osteocytes inhibit NSCLC cell proliferation,
118 osteocyte-conditioned medium (CM) was separated into soluble factor (SF), large extracellular

119 vesicles (lEVs), and small extracellular vesicles (sEVs) fractions by serial ultracentrifugation and
120 ultrafiltration as performed previously with some modifications [27] (Figure 2a). The purified sEVs
121 were verified by transmission electron microscopy (TEM), NanoSight analysis, and
122 immunoblotting for protein markers (CD9, Alix, and TSG101), according to the proposal of the
123 International Society of Extracellular Vesicles (Supplemental Figure 2a – c). sEVs were labeled
124 with PKH67 and were observed to be internalized by NSCLC cells (Supplemental Figure 2d).
125 Subsequently, we treated the NSCLC cells with fractions derived from osteocyte CM, with
126 EV-depleted media as a negative control (fetal bovine serum [FBS] 10%). Interestingly, sEVs
127 from osteocyte CM had a much significantly greater potential to inhibit NSCLC cell proliferation
128 than the other groups (Supplemental Figure 2e, f), whereas sEVs from osteoblast CM had no
129 inhibitory effect on NSCLC cell proliferation (Figure 2 b, c).

130 To confirm the role of sEVs in osteocyte inhibition of NSCLC cell proliferation, GW4869 was
131 used to inhibit sEVs secretion. The significant reduction of sEVs released from MLO-Y4 on
132 GW4869 treatment was confirmed by NanoSight Analysis and western blotting (Figure 2d, e).
133 More importantly, it was found that GW4869 effectively eliminated the inhibitory effect of
134 MLO-Y4 on NSCLC cell proliferation (Figure 2f, g), which suggested that sEVs release was
135 required for osteocytes to inhibit NSCLC cell proliferation. Taken together, osteocytes inhibit
136 NSCLC cell proliferation by releasing sEVs.

137 **Osteocyte sEV miR-99b-3p inhibited NSCLC cell proliferation by directly targeting murine**
138 **double minute2 (MDM2)**

139 Subsequently, we performed micro-RNA (miRNA) sequencing to investigate how
140 osteocyte-derived sEVs inhibit NSCLC cell proliferation. The miRNAs, which can be abundantly

141 encapsulated in sEVs, are key regulators of cancer cell proliferation. To identify the specific
142 miRNAs involved, we compared the miRNA profiles of MLO-Y4-sEVs and MC3T3-E1-sEVs,
143 the results of which are shown as heatmaps (Supplemental Figure 3a). Four of the maximally
144 upregulated miRNAs and two of the downregulated miRNAs were validated by real-time
145 quantitative polymerase chain reaction (qRT-PCR) (Figure. 3a).

146 These four upregulated miRNA sequences are identically conserved in the human and mouse.
147 To determine the effects of these miRNAs on NSCLC cell proliferation, A549 and NCI-H23 cells
148 were transfected with miRNA mimics or negative controls. We found that both miR-99b-3p and
149 miR-193a-5p significantly inhibited NSCLC cell proliferation 48 h after transfection (Figure 3b),
150 with miR-99b-3p having the most significant inhibitory effect. Inhibitors of miR-99b-3p, by
151 contrast, promoted NSCLC cell proliferation (Figure 3c, d). These data indicated that sEVs
152 released by osteocytes carried tumor suppressor miRNAs, such as miR-99b-3p.

153 Notably, in situ hybridization analysis demonstrated high miR-99b-3p expression in the cortical
154 bone of patients with bone metastases of NSCLC (Supplemental Figure 3b). To identify the
155 targets of miR-99b-3p, first, we applied PicTar and TargetScan to search for putative targets,
156 and > 100 mRNAs were predicted to be regulated by miR-99b-3p. Among these candidates, six
157 genes are involved in cell cycle or proliferation regulation. To determine whether miR-99b-3p
158 targets these genes directly, we cloned the 3'UTRs of the putative target into a dual luciferase
159 assay system. MDM2, as a negative regulator of p53, has been shown to exert oncogenic activity
160 [28]. A reporter assay using A549 cells revealed that miR-99b-3p significantly repressed MDM2
161 3'UTRs. Mutations of the putative miRNA sites in MDM2 3'UTRs abrogated the responsiveness
162 to miRNA (Figure 3e). Furthermore, transfection of miR-99b-3p mimicked reduced endogenous

163 MDM2 protein levels in A549 cells. By contrast, inhibition of miR-99b-3p significantly increased
164 the MDM2 protein level (Figure 3f).
165 Taken together, these results suggested that miR-99b-3p derived from osteocyte sEVs directly
166 down-regulates MDM2 expression through its 3'UTR, by which osteocytes inhibited NSCLC cell
167 proliferation.

168 **Mechanical stimulation increased osteocyte sEV release and enhanced the inhibitory effect**
169 **of osteocytes on NSCLC cell proliferation**

170 Osteocytes are thought to be the principal mechanosensors of bone by translating mechanical
171 stimuli into molecular signals and appropriately controlling the downstream remodeling balance.
172 Exercise has the potential to improve physical function and the quality of life in individuals with
173 bone metastases. To determine whether osteocytes inhibit tumor proliferation by receiving
174 mechanical stimulation, MLO-Y4 cells were subjected to sinusoidal stretching at 12% strain at a
175 1.25 Hz frequency for 12 h, and sEVs were extracted from the CM. Interestingly, sEVs released
176 from mechanically-stimulated MLO-Y4 cells significantly inhibited NSCLC cell proliferation
177 compared to static osteocyte sEVs (Figure 4a, b). Notably, the concentration of sEVs of
178 mechanically-stimulated osteocytes was much significantly higher than that of static osteocyte
179 sEVs (Figure 4c, d). Moreover, the miR-99b-3p content of osteocyte sEVs increased significantly
180 after stretching (Figure 4e).
181 To identify the effect of mechanical stimulation on bone metastasis of lung cancer in vivo,
182 mechanical loading (1 N at 2 Hz for 10 min per day, 5 days per week for four weeks) was applied
183 to the tibiae with bone metastasis induced by direct tibial implantation of GFP-LLC in mice. The
184 biophotonic imaging showed that tumor growth was inhibited by mechanical loading (Figure 4f).

185 Consistent with this, Ki-67 expression in NSCLC cells in the mechanical loading group was much
186 lower than that of the control group, which indicated that mechanical loading could effectively
187 inhibit tumor growth (Figure 4g). The micro-CT analysis of the proximal tibia showed that the
188 mechanical loading effectively protected bone integrity and delayed its destruction in the presence
189 bone metastasis in NSCLC, specifically reflected in the BV/TV, Tb.Th, and cortical bone
190 thickness (Figure 4h). Taken together, these results suggested that mechanical stimulation
191 enhanced the inhibitory effect of osteocytes on bone metastasis progression by increasing the
192 release of sEVs containing proliferation-suppressive miRNA.

193 **Moderate exercise combined with zoledronic acid effectively suppressed bone metastasis**
194 **progression of NSCLC**

195 Exercise is one of the ways in which the body senses mechanical stress, so we evaluated the effect
196 of exercise in a mouse bone metastasis model. An intraosseous mouse model was used to
197 investigate the biological progression of NSCLC cells in a bone microenvironment by direct tibial
198 implantation of murine Lewis lung carcinoma (LLC) cells expressing green fluorescent protein
199 (GFP). These mice were subsequently randomized into tumor-bearing only (control), zoledronic
200 acid (ZA), treadmill running, and treadmill running combined with ZA (treadmill running+ZA)
201 groups. Moderate exercise was provided by treadmill running for mice, which were involuntarily
202 placed on a 12-lane rodent treadmill for 30 min per day at a speed of 15cm/s for at least 5 days per
203 week, and were euthanized after 4 weeks. Biophotonic imaging showed that tumor progression in
204 the three treated groups was significantly slower than that in the control group, among which, the
205 treadmill running+ZA group suppressed the growth of tumors in the tibia most effectively (Figure
206 5a). Tumor growth inhibition by the ZA and treadmill running groups was similar, with no

207 statistical difference. Ki-67 protein has been widely used as a proliferation marker for tumor cells.
208 In this study, immunofluorescence assessment results of Ki-67 were largely consistent with those
209 of biophotonic imaging (Figure 5b). The Ki-67 expression level was the lowest in the treadmill
210 running+ZA group lung cancer cells in the tibia, which confirmed that in the treadmill
211 running+ZA group, tumor growth in the tibia was suppressed most effectively. Dentin matrix
212 protein 1 (DMP1), specifically expressed in osteocytes, was used as a specific molecular marker
213 of osteocytes in this study. The micro-computed tomography (microCT) analysis showed that
214 treadmill running and/or ZA protected bone integrity and delayed bone destruction in the presence
215 of bone metastasis in NSCLC, among which, the treadmill running+ZA group displayed the
216 strongest effect, specifically reflected in the bone volume / total volume (BV/TV), trabecular
217 thickness (Tb.Th), and cortical thickness (Ct.Th) (Figure 5c–e). The protective effect of bone
218 integrity in the ZA and treadmill running groups was similar, with no statistical difference. Taken
219 together, these results demonstrated that moderate exercise significantly suppressed bone
220 metastasis progression of NSCLC. Furthermore, moderate exercise combined with ZA displayed
221 additive effects.

222 **Exercise preconditioning effectively suppressed bone metastasis progression of NSCLC**

223 Physical exercise offers therapeutic potentials for bone metastasis. However, it remains mostly
224 unknown whether and how exercise preconditioning affects bone metastasis progression. In this
225 study, we examined the effects of preconditioning on bone metastasis progression in mature adult
226 mice using treadmill running. Male, 8-week-old C57BL/6J mice were subjected to 4 weeks of
227 treadmill exercise followed by tibial implantation of NSCLC cells. Mice were randomized into
228 tumor-bearing only (control), treadmill running before and after tibial implantation of NSCLC

229 cells (exercise preconditioning), and treadmill running after tibial implantation of NSCLC cells
230 (treadmill running) groups. The biophotonic imaging showed that tumor growth in the two
231 exercise groups was significantly slower than that in the control group, with the exercise
232 preconditioning group suppressing the tumor growth more significantly effectively than treadmill
233 running only after tibial implantation of NSCLC cells, which were consistent in C57BL/6J and
234 nude mice (Figure 6a). Regarding the proliferation marker, the Ki-67 immunofluorescence
235 assessment results were largely consistent with those of the biophotonic imaging (Figure 6b). The
236 Ki-67 expression level in NSCLC cells in the exercise preconditioning group was much
237 significantly lower than that in the other groups, which indicated that exercise preconditioning
238 could effectively inhibit tumor growth. The micro-CT analysis showed that the exercise protected
239 bone integrity and delayed bone destruction in the presence of bone metastasis in NSCLC, with
240 the exercise preconditioning group having a stronger effect than the other group, specifically
241 reflected in the BV/TV, Tb.Th, and cortical bone thickness (Figure 6c–e). The micro-CT analyses
242 of C57BL/6 mice and nude mice were consistent. Therefore, these results suggested that
243 maintaining exercise habits may effectively prevent bone metastasis of NSCLC.

244

245 **Discussion**

246 Although many preclinical and clinical studies have shown that exercise can inhibit bone
247 metastasis progression [11,15], the mechanism remains poorly understood. Clarifying the mechanism
248 of action is essential to determine optimal exercise programs, design appropriate combination
249 therapy with standard therapy regimens, or identify specific targets for new treatment. In this
250 study, we found that NSCLC cells adjacent to bone tissue had a much lower proliferative capacity
251 than the surrounding tumor cells, thus we hypothesized that bone tissues release some substance
252 that inhibits tumor growth and sustains tumor dormancy in bone metastasis. Next, we

253 demonstrated that osteocytes inhibit NSCLC cell proliferation by releasing sEVs containing tumor
254 suppressor miRNAs, such as miR-99b-3p. Meanwhile, both in vitro and in vivo experiments
255 demonstrated that mechanical loading stimulated osteocytes to release more sEVs and
256 miR-99b-3p to delay the progression of bone metastasis of NSCLC. In addition, we showed that
257 bone metastasis progression of NSCLC was inhibited by moderate exercise, and combinations
258 with ZA had additive effects. Furthermore, exercise preconditioning effectively suppressed bone
259 metastasis progression of NSCLC. Taken together, our work elucidated a mechanism for the
260 clinical observation that bone metastasis was inhibited by moderate exercise.

261 In bone metastasis, only a limited number of disseminated tumor cells survive following bone
262 colonization, and these are retained in a dormant state for prolonged periods through engagement
263 in specialized endosteal niches before becoming reactivated to form overt metastases [5]. Currently,
264 molecular mechanisms for tumor cell dormancy in the endosteal niche remain poorly understood,
265 representing both a challenge and an opportunity for therapeutic targeting [29]. Bone metastases
266 occur from a complex interplay between cancer cells and bone cells. Interestingly, here we found
267 that NSCLC cells adjacent to bone tissue have a much lower proliferative capacity than the
268 surrounding tumor cells. Therefore, we hypothesized that bone tissues release some substance that
269 inhibits tumor growth and sustains NSCLC cell dormancy in bone metastasis.

270 Osteoclast and osteoblast functions in bone metastases have been well characterized; however,
271 the role of osteocytes needs to be elucidated [30]. Osteocytes act as mechanosensors to control
272 responses to mechanical loading of the skeleton. For bone metastases, osteocytes may play a
273 pivotal role in the interaction between mechanical loading and SREs. Here we demonstrated that it
274 is osteocytes that inhibit NSCLC cell proliferation in the endosteal niche, but not osteoblasts.
275 Furthermore, we demonstrated that osteocytes inhibit NSCLC cell proliferation by releasing sEVs
276 containing tumor suppressor miRNAs, such as miR-99b-3p. Recent studies showed that
277 miR-99b-3p functions as a potential tumor suppressor in oral squamous cell carcinoma and gastric
278 cancer [31,32]. We found that osteocyte sEV miR-99b-3p inhibited NSCLC cell proliferation by
279 directly targeting MDM2. As a negative regulator of the p53, the most extensively studied human
280 tumor suppressor, MDM2 has been shown to exert oncogenic activity [28]. To date, three regions of
281 interaction between MDM2 and p53 have been identified, by which MDM2 inhibits the binding of

282 p53 to the transcriptional machinery. MDM2 is significantly highly expressed in lung
283 adenocarcinoma tissues compared with adjacent tissues, and is regarded as a proto-oncogene [33,34].
284 Our findings identified MDM2 as a direct target of miR-99b-3p, emphasizing the crucial role of
285 miRNA in bone metastases. Interestingly, the miR-99b-3p content in osteocyte sEVs increased
286 dramatically after mechanical loading, suggesting that miR-99b-3p may play a role in the
287 inhibition of bone metastases by exercise.

288 SREs resulting from bone metastasis are a major clinical problem that significantly harm patient
289 outcomes, and are commonly considered an incurable consequence of terminal malignancies.
290 Bone metastases from lung cancer represent the majority of cases, followed by prostate cancer and
291 breast cancer [35]. A recent animal study showed that in vivo exercise was protective against
292 metastatic bone loss and inhibited breast cancer progression in bone [36]. However, there was no
293 report about the effect of exercise on bone metastasis of lung cancer until recently. In the present
294 study, we showed that bone metastasis progression in lung cancer was inhibited by exercise. More
295 interestingly, exercise preconditioning effectively suppressed bone metastasis progression of
296 NSCLC, suggesting that maintaining exercise habits affords protection against bone metastasis.
297 Bisphosphonates are the standard of care in patients with bone metastases. Our study
298 demonstrated that moderate exercise and ZA have additive effects.

299 Exercise is quite complex because it involves multiple organs of the body. The bone can sense
300 the mechanical stress stimulus in the process of exercise. Using in vivo models, mostly breast
301 cancer bone metastasis models, several studies suggested that mechanical stimulation of the tibia
302 can contribute to inhibiting bone metastatic colonization and cancer progression in bone [36,37].
303 Tibial compression has been used to stimulate bone formation and study the interplay between
304 mechanical stimuli and SREs. One study showed that moderate tibial loading, but not overloading,
305 protected adult murine bone from destruction by metastasized breast cancer [36]. Consistent with
306 this, our work showed that mechanical loading of the tibia inhibited bone metastasis progression
307 of NSCLC. Although many preclinical and clinical studies have shown that exercise can inhibit
308 cancer progression, the ideal mechanism of implementation remains to be determined. The
309 prescription of exercise for patients with cancer requires further research, including exercise type,
310 frequency, duration, intensity, and whether it is supervised [14,16]. Exercise has been underutilized in

311 patients with advanced cancer despite the benefits, particularly for those with bone metastases
312 because of concerns over skeletal complications [38,39]. Multiple studies showed that individuals
313 with NSCLC were engaged in significantly less physical activity than similar-aged healthy
314 individuals [40,41]. Exercise models such as running are more realistic for healthy people, but
315 mechanical loading such as tibial compression provides for isolating the impacts of mechanical
316 stimuli on bone tissue in the context of SREs, which are more effective and safer for patients with
317 advanced cancer.

318 In conclusion, our study provides new insights into understanding the mechanism underlying
319 exercise-afforded protection against bone metastasis progression. Bone metastasis progression of
320 NSCLC was inhibited by moderate exercise. Osteocytes, sensing mechanical stimulation
321 generated by exercise, inhibit the proliferation of NSCLC cells and sustain their dormancy by
322 releasing sEVs containing tumor-suppressive miRNAs (Figure 7). Understanding the mechanism
323 underlying tumor dormancy may provide the foundation for the development of strategies to
324 prevent dormant bone metastasis from emerging as overt bone metastasis.

325

326 Materials and Methods

327 Patients

328 Lung cancer patients with a diagnosis of bone metastases (six patients, radiologically confirmed)
329 were recruited by the Third Affiliated Hospital of Southern Medical University (Guangzhou,
330 China) from January 2020 to January 2021. All patients were fully informed of the study, and they
331 provided written consent prior to participation. Surgically resected bone metastatic tumor tissue
332 was collected from all patients. The obtained bone metastatic tumor tissue was trimmed to an
333 appropriate size and rapidly transferred to formalin solution for storage until processing. We
334 confirm that our study was compliant with the "Guidance of the Ministry of Science and
335 Technology (MOST) for the Review and Approval of Human Genetic Resources". Ethics

336 approval was granted by the Human Research Ethics Committee of the Third Affiliated Hospital
337 of Southern Medical University. The study was conducted in accordance with the principles and
338 guidelines of The Declaration of Helsinki.

339 **Cell lines**

340 A549, LLC, and MLO-Y4 cells were purchased from the American Type Culture Collection
341 (Rockville, MD, United States) and grown in dulbecco's modified eagle medium (DMEM)
342 (Invitrogen, Waltham, MA, United States) containing 10% FBS and 1% penicillin and
343 streptomycin. MC3T3-E1 cells were purchased from the American Type Culture Collection and
344 were cultured in α Minimum Essential Medium (α-MEM) (Invitrogen) with 10% FBS and 1%
345 penicillin and streptomycin. These cell lines were not authenticated after purchase but routinely
346 tested negative for mycoplasma contamination.

347 **Animal models**

348 All animal experimental protocols were approved by the Animal Care and Use Committee of the
349 Southern Medical University, Guangzhou, China. C57BL/6 and nude athymic mice were obtained
350 from the Experimental Animal Center of the Southern Medical University in Guangzhou, China.
351 Animal care was in accordance with the guidelines of the US National Institutes of Health and the
352 Chinese National Institute of Health. All surgical interventions were performed under anesthesia
353 with a mixture of 13.3% urethane and 0.5% chloralose (0.65 ml/100 g body weight). All efforts
354 were made to reduce the number of animals used and to minimize animal discomfort.

355 For in situ studies, 25×10^4 LLC cells or A549 cells were injected into the tibiae of 8-week-old
356 C57BL/6 mice or nude mice. In brief, 25×10^4 LLC cells and A549 cells suspended in
357 phosphate-buffered saline (PBS) were injected into the tibia of C57BL/6 mice and nude mice,

358 respectively. Mice were euthanized on day 21 for analyses, unless otherwise indicated. For
359 stress-induced experiments, after 2 days of recovery, tibiae loading was performed daily on the
360 tumor-inoculated tibiae. Using an ElectroForce device (Bose, Framingham, MA, United States),
361 the tibiae of the mask-anesthetized mice were given daily loads of 1 N (peak-to-peak) at 2 Hz for
362 10 min, 5 days per week for 4 weeks.

363 For zoledronic acid experiments, starting on day 3 after lung cancer cell transplantation, mice
364 were treated with subcutaneous injection of 100 μg/kg zoledronic acid (Novartis, Basel,
365 Switzerland) or saline (other groups) every 3 days for 3 weeks, after which they were euthanized.
366 For exercise experiments, exercised mice were involuntarily placed on a 12-lane rodent treadmill
367 for 30 min per day at a speed of 15 cm/s for at least 5 days per week unless otherwise stated.
368 During the 3 days prior to euthanasia, the exercising mice underwent obligatory exercise,
369 regardless of how many consecutive days they had previously exercised. Two days after surgery,
370 all mice except the control group began moderate exercise by treadmill running, whereby they
371 were involuntarily placed on a 12-lane rodent treadmill for 30 min per day at a speed of 15 cm/s
372 for at least 5 days per week, and were euthanized after 4 weeks. For exercise preconditioning,
373 mice were additionally subjected to 4 weeks of treadmill exercise prior to tibial implantation of
374 NSCLC cells. In the matched experiment, the control mice were placed on a stationary (0 cm/s)
375 treadmill for the same time duration as the experimental mice.

376 We examined the effects of preconditioning on bone metastasis progression in mature adult
377 mice using treadmill running. Male 8-week-old C57BL/6J mice were subjected to 4 weeks of
378 treadmill exercise followed by tibial implantation of NSCLC cells.

379 **Lung cancer cell preparation and in situ injection**

380 We used clones derived from the GFP-tagged LLC cells and A549 cells. The cells were
381 maintained in DMEM containing 10% FBS and 0.1 mg/ml penicillin-streptomycin at 37 °C under
382 5%–8% CO_2. Cells were passaged at 80%–90% confluence and re-plated at a 1:10 dilution, which
383 was approximately every 72 h. Before in situ injection, cells were trypsinized at 80%–90%
384 confluence with 0.15% trypsin / ethylene diamine tetraacetic acid (EDTA) (0.5% Gibco trypsin
385 EDTA diluted 1:2 in PBS). Cells were immediately removed from the plate with 10 ml ice-cold
386 DMEM containing 10% FBS, pipetted into a 15 ml conical tube, and centrifuged at 200 × g for 5
387 min. The pellet was resuspended in a 50 ml conical tube in 25 ml ice-cold PBS (without Ca or Mg)
388 and counted. This was centrifuged to re-pellet, and finally resuspend at 25 × 10^4 cells/10 μl in
389 ice-cold PBS.

390 The mice were anesthetized using a mixture of 13.3% urethane and 0.5% chloralose (0.65
391 mL/100 g body weight). Both legs were cleaned with 10% povidone/iodine swab/solution,
392 followed by ethanol, repeated twice. The skin was wetted with 70% ethanol to increase visibility
393 of the underlying patellar ligament, which should be visible as a distinct, thick, white line. While
394 firmly grasping the ankle/leg of the mouse, a 28g ½ needle was inserted under the patella, through
395 the middle of patellar ligament, and into the anterior intercondylar area in the top of the tibia. A
396 gentle, lateral movement of the needle was applied to ensure it was in tibia and passed through the
397 growth plate. The plunger was slowly depressed to inject 10 μl of cell solution. After 3 min, the
398 needle was slowly extracted. The treated mice were kept on a heating pad until revived.

399 **Mechanical stress stimulation of MLO-Y4 cells**

400 MLO-Y4 cells were transferred to a Biofex six-well plate (Flexcell, Burlington, NC, USA) and
401 allowed to adhere to the membrane until they attained 90% confluence. The cells were subjected

402 to sinusoidal stretching (Flexcell) at 12% strain and 1.25 Hz frequency for 12 h. Experiments were
403 performed at 37 °C under 5% CO_2. Following 48 h of stretching, the CM (or control medium) was
404 collected for sEV extraction.

405 **Bio-photon imaging and micro-CT imaging**

406 Tumor-bearing mice were euthanized 30 days after tumor cell injection, and their hind limb bones
407 were imaged by biophotonics. Fluorescence imaging for GFP-labeled tumor cells in these bones
408 was performed using the optical imaging system, Fx Pro (Bruker BioSpin MRI GmbH, Ettlingen,
409 Germany). For anatomical orientation, a white light/grayscale picture was performed and used
410 with the fluorescent signal (Cy3.5: excitation = 570 nm; emission = 620 nm). For data analysis,
411 molecular imaging software 7.1.3 (Bruker BioSpin MRI GmbH) was used. Regions of interest
412 (ROIs) were defined around the bone and analyzed compared to the background of PBS injection
413 to calculate the signal to noise ratio.

414 Micro-CT was performed using the Skyscan 1172 (Bruker-MicroCT, Kontich, Belgium). The
415 X-Ray tube settings were 80 kV and 500 μA and images were acquired at the highest resolution
416 without charge coupled device binning, resulting in a voxel size of 9.44 μm. A 0.66° rotation step
417 through a 195° angular range with 6500 msec exposure was used. After processing with a
418 three-dimensional Gaussian filter to reduce noise, the ROIs were manually segmented such that
419 they corresponded to the cortical and trabecular bone regions. Cortical ROIs comprised 470 μm
420 thick regions (50 slices, 9.4 μm thickness per slice) located 3 mm distal to the growth plate, while
421 300 μm thick trabecular sections began 0.27 mm distal to the growth plate.

422 **Histological analysis, immunohistochemistry, and immunofluorescence staining**

423 Bone samples were fixed in 4% paraformaldehyde in PBS and decalcified in a 10% EDTA

424 solution. They were subsequently dehydrated through a series of graded alcohols, cleared in
425 xylene, and embedded in paraffin. Sagittal sections of 2–5 μm were prepared for histological
426 analyses. Following deparaffinization and rehydration, H&E staining were performed on the tissue
427 sections. The tissue sections were imaged using an FSX100 microscope (Olympus, Tokyo, Japan).
428 For immunohistochemistry, sections were incubated in 10 mM citrate buffer (pH 6.0) for 30
429 min at 90 °C or treated with 200 mg/mL proteinase K (Sigma Aldrich, St. Louis, MO, United
430 States) for 10 min at 37 °C to unmask antigen. Subsequently, the sections were treated with 3%
431 hydrogen peroxide for 15 min. Thereafter, the sections were permeabilized with 0.1% Triton
432 X-100 in PBS for 5 min at room temperature and blocked with 1% sheep serum at room
433 temperature for 1 h. We incubated the sections with a primary antibody that recognized Ki67 (Cell
434 Signaling Technology, Danvers, MA, United States, cat. #: 9129, 1:200) overnight at 4 °C.
435 Subsequently, we used a horse radish peroxidase-labeled secondary antibodies (1:200 in 1%
436 bovine serum albumin [BSA], 1 h) at 37°C. Diaminobenzidine was used as a chromogen and
437 hematoxylin as the counterstain.
438 For immunofluorescence, we incubated primary antibodies that recognized Ki67 (Cell
439 Signaling Technology, cat. #: 9129, 1:200) and DMP1 (R&D Systems, Minneapolis, MN, United
440 States, cat. #: AF4386, 1:100) overnight at 4 °C. For secondary reactions, species-matched Alexa
441 Fluor 488- and Alexa Fluor 594-secondary antibodies were used (1:500 in 1% BSA, 1 hour) at
442 37 °C in the dark. The secondary antibodies for immunofluorescence staining were goat
443 anti-rabbit Alexa Fluor 488 (Invitrogen, cat#A-11008) and donkey anti-Sheep Alexa Fluor 594
444 (Invitrogen, cat#A-11016). The sections were mounted with 4',6-diamidino-2-phenylindole (DAPI)
445 (Thermo Fisher, Waltham, MA, United States) before imaging and we examined more than five

446 different microscopic images (per section) under a confocal laser scanning microscope (Olympus,
447 Tokyo, Japan).

448 **Western blot analysis.**

449 Cells and sEVs were lysed with 2% Sodium dodecyl sulfonate (SDS), 2 M urea, 10% glycerol, 10
450 mM Tris-HCl (pH 6.8), 10 mM dithiothreitol, and 1 mM phenylmethylsulfonyl fluoride. The
451 lysates were separated by SDS-polyacrylamide gel electrophoresis and blocked with BSA.
452 Following blotting onto a nitrocellulose membrane (Bio-Rad Laboratories, Hercules, CA, United
453 States), the membrane was incubated with primary antibodies that recognized TSG101 (Abcam,
454 Cambridge, United Kingdom cat. #: ab83, 1:1,000), CD63 (Abcam, cat. #: ab193349, 1:1,000),
455 CD9 (Abcam, cat. #: ab223052, 1:1,000), Alix (Abcam, cat. #: ab76608, 1:1,000), β-actin (Cell
456 Signaling Technology, cat. #: 4970S, 1:4000), MDM2 (Proteintech, Wuhan, China cat. #:
457 66511-1-IG, 1:1000), and GAPDH (Cell Signaling Technology, cat. #: 2118, 1:5000) overnight at
458 4 °C. Secondary antibodies for western blot were anti-rabbit IgG, (cat# 7074, dilution 1:2000)
459 from Cell Signaling Technology and anti-mouse IgG, (cat# A9044, dilution 1:2000) from Sigma
460 Aldrich (1 hour at 37 °C). The membrane was analyzed using specific antibodies and visualized
461 using an enhanced chemiluminescence 50 kit (Amersham Biosciences, Piscataway, NJ, United
462 States).

463 **Transwell assay.**

464 The migration capacity of cancer cells was determined using a 24-well plate, Transwell chambers
465 (Thermo Fisher) with an 8-μm pore size, and Matrigel (100 $\mu g \cdot mL^{-1}$). Approximately 5×10^4
466 cells in 200 μL serum-free DMEM were plated in the upper chambers, and 800 μL CM was added
467 to the lower chambers. After 48 h, the cells that had invaded to the lower side of the membrane

468 were stained with crystal violet. At minimum of five randomly selected images were acquired, and
469 the mean number of stained cells was determined.

470 **Luciferase assays.**

471 A549 cells were cultured at 1×10^5 cells/well in 12-well plates. The cells were co-transfected with
472 miR-99b-3p mimic (50 nM) or miRNA mimic negative control (50 nM) and 0.2 μg
473 psiCHECK™-1-UTR. Transfection was performed using Lipofectamine 3000. After 48 h, cells
474 were collected and luciferase activity was determined using the DualLuciferase reporter assay
475 system (Promega, Madison, WI, United States) with the dual luciferase assay reporter-ready
476 luminometer (Promega). The assays were performed in triplicate.

477 **TEM and nanosight tracking analysis.**

478 The morphology of the sEVs was observed by TEM. Briefly, the sEV suspension was mixed with
479 an equal amount of 4% paraformaldehyde. Following washing with PBS, 4% uranyl acetate was
480 added for chemical staining of sEVs, and images were captured using a Hitachi H-7650 TEM
481 (Hitachi, Tokyo, Japan). Nanosight tracking analysis was performed to determine the size and
482 concentration of the isolated sEVs using the NanoSight NS500 (Malvern, Westborough, MA,
483 United States), according to the operating instructions, without any changes. The sEVs were
484 diluted to be within the recommended concentration range. Five 60 s videos were captured for
485 each sample during flow mode (camera settings: slider shutter 890, slider gain 146).
486 Plasma-derived sEVs were diluted and loaded onto the NS500 instrument by a syringe. The videos
487 were analyzed with the NTA 3.2 software (Malvern). All measurements were performed at room
488 temperature.

489 **RNA isolation**

490 RNA was extracted from cells using the QIAzol Lysis Reagent (Qiagen, Hilden, Germany)
491 according to the user guidelines. Briefly, cells were collected in a reaction tube, lysed with QIAzol,
492 and mixed with chloroform. Following centrifugation at 12,000 × g for 15 min at 4 °C, the upper
493 aqueous phase was transferred to an RNeasy Mini spin column in a 2 mL collection tube and
494 mixed with 100% ethanol. Following washing at 7500 × g for 5 min at 4 °C, the total RNA was
495 collected for qRT-PCR analysis. RNA was extracted from plasma and sEV fractions using the
496 Qiagen miRNeasy Mini kit (Qiagen) according to the manufacturer's instructions, with a final
497 elution volume of 50 μL.

498 **MiRNA sequencing**

499 Total RNA extraction from the samples was conducted using the miRNeasy Kit (Qiagen),
500 according to standard operating procedures provided by the manufacturer. The quality and
501 integrity of the total RNA were determined using the Agilent 2100 Bioanalyzer and the RNA 6000
502 Nano LabChip Kit (Agilent, Santa Clara, CA, United States). A sequencing RNA library was
503 constructed by performing a 3′-end linker, a 5′-end linker, reverse transcription, amplification,
504 cDNA library size selection, and purification steps using total RNA. Cluster generation and first
505 stage sequencing primer hybridization were performed on the cBot of the Illumina HiSeq
506 sequencer from Shanghai Biotechnology (Shanghai, China), according to the corresponding
507 procedure in the cBot User Guide. Subsequently, the sequencing reagent was prepared following
508 the Illumina User Guide and the flow cell carrying the cluster was loaded into the machine.
509 Single-end sequencing was performed using the single-read program. The sequencing process was
510 controlled by the data collection software provided by Illumina that performed real-time data
511 analyses.

512 **RT-PCR and qRT-PCR**

513 RNA samples were quantitated and qualified using a NanoDrop analyzer (ThermoFisher). Equal
514 quantities (5 ng) of total RNA from each sample were used for cDNA synthesis using the
515 PrimeScript®RT reagent kit (TaKaRa, Tokyo, Japan). The reverse transcriptions of miRNAs were
516 performed using looped miRNA-specific RT primers for miRNAs. qRT-PCR was performed with
517 the Step One Plus (Applied Biosystems, Carlsbad, CA, United States, using an SYBR Green I
518 Real-Time PCR Kit (GenePharma, Shanghai, China) for miR-99b-3p. Dissociation curves were
519 generated to ensure the specificity of each qRT-PCR reaction. The relative expression levels of
520 miRNAs in each sample were calculated and quantified using the $2^{-\Delta\Delta CT}$ method after
521 normalization for expression of the positive control.

522 **Co-culture experiments**

523 Well inserts with a 0.4 mm pore size filter (BD Falcon, Franklin Lake, NJ, United States) for
524 six-well plates were used following the manufacturer's instructions. MLO-Y4 and MC3T3-E1
525 cells were seeded into the well inserts with DMEM medium. LLC, A549, and MLO-Y4 cells were
526 also seeded into six-well plates. All co-culture experiments were conducted in DMEM with
527 sEV-free FBS (Life Technologies, Carlsbad, CA, United States).

528 **Differential ultracentrifugation of several fractions from CM and sEV isolation**

529 To isolate the different EV fractions, 1×10^6 cells were plated in a 10 cm dish (10 ml medium).
530 After 72 h we either separated the conditioned media or isolated sEVs. For the dissection of the
531 CM, whole CM (10 ml for one 10 cm dish) was collected by pipetting from the 10 cm dish into 50
532 mL falcon tubes, centrifuged at low speed (2,000 × g for 20 min) to eliminate dead cells and
533 cellular debris prior to use, and divided into two. One half was used as whole CM, concentrated

534 with a 10 KD ultrafiltration device (Millipore, Billerica, MA, United States) at 5000 × g for 15
535 min and were transferred to 12 wells of a 96-well plate, while the remaining half was further
536 processed. From the second half, lEVs were collected after a 10,000 × g centrifugation step for 1 h,
537 washed in 15 mL PBS, and centrifuged again at 10,000 × g for 1 h. The SF was filtered through a
538 0.22 mm filter prior to a 100,000 × g centrifugation step. The SF was collected after a 80 min
539 100,000 × g centrifugation step and concentrated using a 10 KD ultrafiltration device (Millipore)
540 at 5000 × g for 15 min, obtaining concentrated factor. The final 100,000 × g pellet (sEVs) was
541 washed once in 15 ml PBS and resuspended in 10% EV-depleted FBS medium for the functional
542 cell culture experiments. Each individual SF, lEV, and sEV fraction was used were transferred to
543 12 wells of a 96-well plate. SEVs from 10 ml of conditioned media were added either to 6 wells of
544 a 96-well plate or one well of a 12-well plate. Media with EV-depleted serum (10% FBS) was
545 used as a negative control in most experiments.

546 **Cell counting kit-8 assay**

547 The Cell Counting Kit-8 assay (CCK-8) was used to determine cell viability. In total, 2×10^3 cells
548 were seeded in 96-well plates and allowed to adhere overnight. Following incubation with the
549 compounds under evaluation for 72 h, 10 μL CCK-8 dye was added to each well, and the cells
550 were incubated for 1 h at 37 °C. Subsequently, the absorbance was determined at 450 nm (BioTek
551 Synergy-HTX, Winooski, VT, United States).

552 **Flow cytometry**

553 Approximately 10,000 cells were seeded in 12-well plates on day 1. Treatment was added on day
554 2, and cell proliferation was examined using a fluorescence-based cell proliferation kit (Cell-Light
555 EdU Apollo488 In Vitro Flow Cytometry Kit, Ribobio, Guangzhou, China) on day 4. Following

556 fluorescence labeling, the ratio of the number of fluorescently labeled cells to the total number of
557 cells was determined by flow cytometry (Beckman, Brea, CA, United States).

558 **SEVs labeling and cellular uptake**

559 SEVs were labeled using the PKH67 Green Fluorescent Cell Linker Kit (Sigma-Aldrich) by
560 following the manufacturer's protocol. The isolated sEVs diluted in PBS was added to 0.5 mL
561 Diluent C. Subsequently, 2 μL PKH67 dye was added and incubated for 4 min at room
562 temperature. Two milliliters of 1% BSA/PBS was added to bind excess dye. The labeled sEVs
563 were washed at 100,000 × g for 70 min, and the sEV pellet was suspended in PBS and used for
564 uptake experiments. We subsequently co-cultured these PKH67 sEVs with A549. After the
565 indicated time of co-culture, we stained the A549 with DAPI (Sigma-Aldrich) and observed them
566 by confocal microscopy.

567 **Statistical analysis**

568 All data were analyzed for statistical significance using GraphPad Prism 6.0 software (GraphPad
569 Software, San Diego, CA, United States). The P value was determined by the Student's t-test for
570 two-group, or one-way analysis of variance test for multiple group comparisons. It was considered
571 indicative of statistical significance when $P < 0.05$. All experiments were repeated a minimum of
572 three times. Quantitative data were expressed as mean ± standard error of the mean.

573 **Data availability statement**

574 All data generated or analyzed during this study are included in this submitted article and its
575 additional files.

576 **Author contributions**

QCS and XCB designed the experiments. JX, YFX, XHL, LL, and JC performed the experiments and analyzed the data. QCS, XCB, and JX wrote the manuscript. YS, RXZ, and JRL assisted with cell culture and in vivo experiments. YFX, ZQC, and ZMZ assisted with the collection of patient samples and editing of the manuscript. All authors contributed to the article and approved the submitted version.

Acknowledgments

We thank the Central Laboratory, Southern Medical University for providing facilities and technical support. This work was supported by grants from the National Natural Science Foundation of China (Grant No. 81991510).

Competing interests

The authors have declared that no conflict of interest exists.

References

1. Sung, H., *et al.* Global cancer statistics 2020: GLOBOCAN estimates of incidence and mortality worldwide for 36 cancers in 185 countries. *Ca-a Cancer Journal for Clinicians* **71**, 209-249 (2021).
2. Herbst, R.S., Morgensztern, D. & Boshoff, C. The biology and management of non-small cell lung cancer. *Nature* **553**, 446-454 (2018).
3. Cetin, K., Christiansen, C.F., Jacobsen, J.B., Norgaard, M. & Sorensen, H.T. Bone metastasis, skeletal-related events, and mortality in lung cancer patients: a Danish population-based cohort study. *Lung Cancer* **86**, 247-254 (2014).
4. Riihimaki, M., *et al.* Metastatic sites and survival in lung cancer. *Lung Cancer* **86**, 78-84 (2014).
5. Zhang, W.J., Bado, I., Wang, H., Lo, H.C. & Zhang, X.H.F. Bone Metastasis: Find Your Niche and Fit in. *Trends in Cancer* **5**, 95-110 (2019).
6. Sowder, M.E. & Johnson, R.W. Bone as a Preferential Site for Metastasis. *JBMR plus* **3**, e10126 (2019).
7. Knapp, B.J., Devarakonda, S. & Govindan, R. Bone metastases in non-small cell lung cancer: a narrative review. *J Thorac Dis* **14**, 1696-1712 (2022).
8. Pedersen, L., *et al.* Voluntary Running Suppresses Tumor Growth through Epinephrine- and IL-6-Dependent NK Cell Mobilization and Redistribution. *Cell Metab* **23**, 554-562 (2016).

9. Schmitz, K.H., *et al.* Exercise is medicine in oncology: Engaging clinicians to help patients move through cancer. *CA: a cancer journal for clinicians* **69**, 468-484 (2019).
10. Bade, B.C., Thomas, D.D., Scott, J.B. & Silvestri, G.A. Increasing physical activity and exercise in lung cancer: reviewing safety, benefits, and application. *J Thorac Oncol* **10**, 861-871 (2015).
11. Ligibel, J.A., *et al.* Exercise, Diet, and Weight Management During Cancer Treatment: ASCO Guideline. *J Clin Oncol* **40**, 2491-2507 (2022).
12. Kerr, J., Anderson, C. & Lippman, S.M. Physical activity, sedentary behaviour, diet, and cancer: an update and emerging new evidence. *Lancet Oncol* **18**, e457-e471 (2017).
13. Cao, C., Friedenreich, C.M. & Yang, L. Association of Daily Sitting Time and Leisure-Time Physical Activity With Survival Among US Cancer Survivors. *JAMA Oncol* **8**, 395-403 (2022).
14. Stout, N.L., Santa Mina, D., Lyons, K.D., Robb, K. & Silver, J.K. A systematic review of rehabilitation and exercise recommendations in oncology guidelines. *CA Cancer J Clin* **71**, 149-175 (2021).
15. Weller, S., *et al.* Exercise for individuals with bone metastases: A systematic review. *Crit Rev Oncol Hematol* **166**, 103433 (2021).
16. Cavalheri, V. & Granger, C.L. Exercise training as part of lung cancer therapy. *Respirology* **25**, 80-87 (2020).
17. Wang, Q.Y. & Zhou, W.L. Roles and molecular mechanisms of physical exercise in cancer prevention and treatment. *J Sport Health Sci* **10**, 201-210 (2021).
18. Zhu, C.M., *et al.* Exercise in cancer prevention and anticancer therapy: Efficacy, molecular mechanisms and clinical information. *Cancer Letters* **544**(2022).
19. Ruiz-Casado, A., *et al.* Exercise and the Hallmarks of Cancer. *Trends in Cancer* **3**, 423-441 (2017).
20. Wang, L.J., You, X.L., Zhang, L.L., Zhang, C.Q. & Zou, W.G. Mechanical regulation of bone remodeling. *Bone Research* **10**(2022).
21. Prideaux, M., Findlay, D.M. & Atkins, G.J. Osteocytes: The master cells in bone remodelling. *Curr Opin Pharmacol* **28**, 24-30 (2016).
22. Schaffler, M.B., Cheung, W.Y., Majeska, R. & Kennedy, O. Osteocytes: master orchestrators of bone. *Calcif Tissue Int* **94**, 5-24 (2014).
23. Robling, A.G. & Bonewald, L.F. The Osteocyte: New Insights. in *Annual Review of Physiology, Vol 82*, Vol. 82 (eds. Nelson, M.T. & Walsh, K.) 485-506 (2020).
24. Clezardin, P., *et al.* Bone metastasis: mechanisms, therapies, and biomarkers. *Physiol Rev* **101**, 797-855 (2021).
25. Phan, T.G. & Croucher, P.I. The dormant cancer cell life cycle. *Nature Reviews Cancer* **20**, 398-411 (2020).
26. Blasco, M.T., Espuny, I. & Gomis, R.R. Ecology and evolution of dormant metastasis. *Trends in Cancer* **8**, 570-582 (2022).
27. Fafian-Labora, J.A., Rodriguez-Navarro, J.A. & O'Loghlen, A. Small Extracellular Vesicles Have GST Activity and Ameliorate Senescence-Related Tissue Damage. *Cell Metab* **32**, 71-+ (2020).
28. Karni-Schmidt, O., Lokshin, M. & Prives, C. The Roles of MDM2 and MDMX in Cancer. *Annual review of pathology* **11**, 617-644 (2016).

29. Clezardin, P., *et al.* Bonemetastasis: Mechanisms, Therapies, and Biomarkers. *Physiological Reviews* **101**, 797-855 (2021).
30. Atkinson, E.G. & Delgado-Calle, J. The Emerging Role of Osteocytes in Cancer in Bone. *JBMR plus* **3**, e10186 (2019).
31. He, K., *et al.* miRNA-99b-3p functions as a potential tumor suppressor by targeting glycogen synthase kinase-3 beta in oral squamous cell carcinoma Tca-8113 cells. *Int J Oncol* **47**, 1528-1536 (2015).
32. Chang, S.E., *et al.* miR-99b-3p is induced by vitamin D3 and contributes to its antiproliferative effects in gastric cancer cells by targeting HoxD3. *Biol Chem* **400**, 1079-1086 (2019).
33. Ni, L.W., *et al.* MiR-221-3p-mediated downregulation of MDM2 reverses the paclitaxel resistance of non-small cell lung cancer in vitro and in vivo. *Eur J Pharmacol* **899**(2021).
34. Chen, B., *et al.* SHANK1 facilitates non-small cell lung cancer processes through modulating the ubiquitination of Klotho by interacting with MDM2. *Cell Death Dis* **13**(2022).
35. Ryan, C., *et al.* Epidemiology of bone metastases. *Bone* **158**(2022).
36. Wang, S., *et al.* Moderate tibial loading and treadmill running, but not overloading, protect adult murine bone from destruction by metastasized breast cancer. *Bone* **153**, 116100 (2021).
37. Fan, Y., *et al.* Skeletal loading regulates breast cancer-associated osteolysis in a loading intensity-dependent fashion. *Bone Res* **8**, 9 (2020).
38. Cheville, A.L., Kornblith, A.B. & Basford, J.R. An examination of the causes for the underutilization of rehabilitation services among people with advanced cancer. *Am J Phys Med Rehabil* **90**, S27-37 (2011).
39. Ten Tusscher, M.R., *et al.* Education Needs of Dutch Physical Therapists for the Treatment of Patients With Advanced Cancer: A Mixed Methods Study. *Phys Ther* **100**, 477-486 (2020).
40. Granger, C.L., Denehy, L., McDonald, C.F., Irving, L. & Clark, R.A. Physical activity measured using global positioning system tracking in non-small cell lung cancer: an observational study. *Integr Cancer Ther* **13**, 482-492 (2014).
41. Granger, C.L., *et al.* Low physical activity levels and functional decline in individuals with lung cancer. *Lung Cancer* **83**, 292-299 (2014).

686 **Figures**

687 **Figure 1**

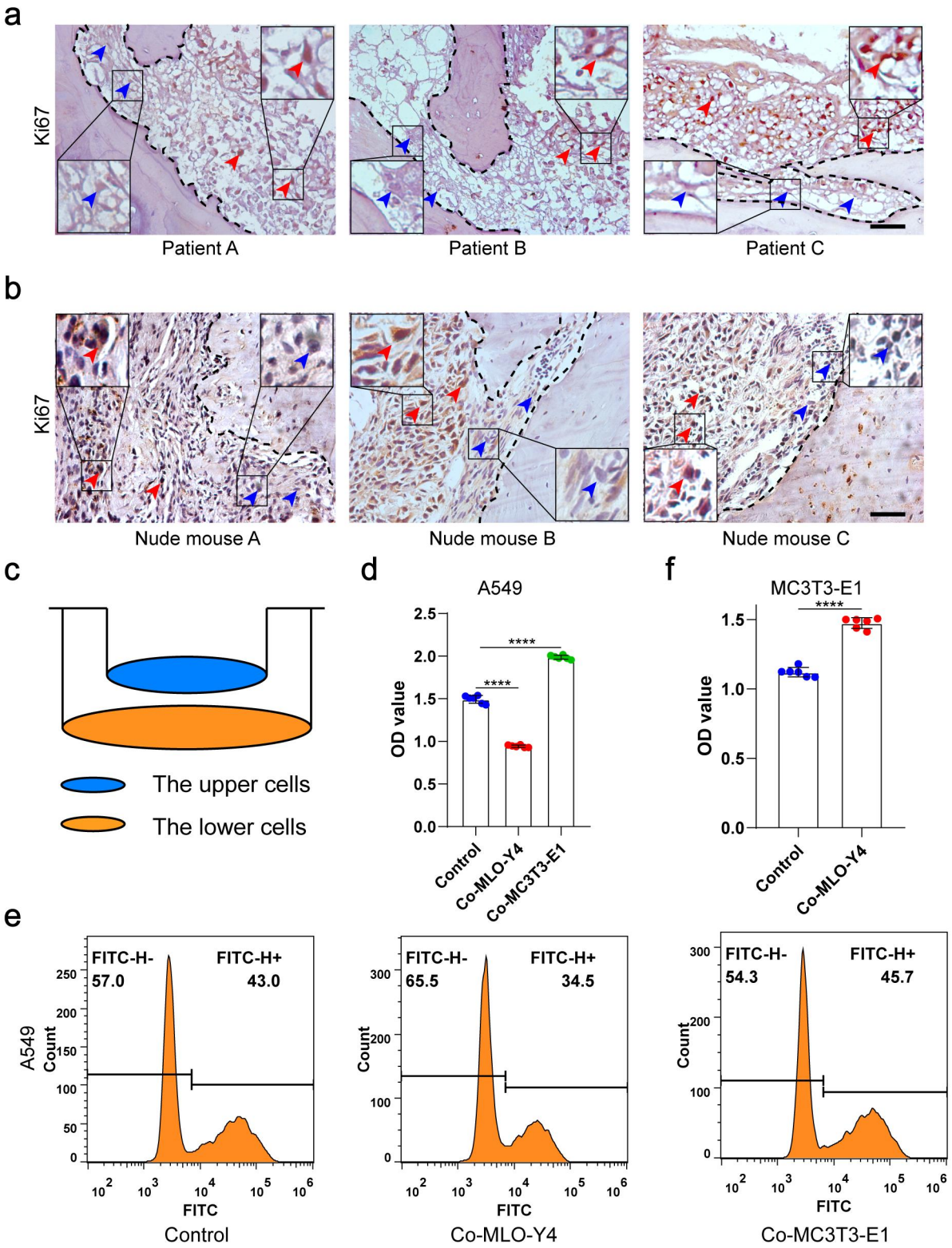

688

689 **Figure 1. Osteocytes inhibited the proliferation of NSCLC cells.**

690 a. Representative immunohistochemical staining of Ki-67 in bone metastasis site of patients with
691 NSCLC. The dashed line indicates the boundary between bone and tumor. Scale bars: 50 μm.
692 Blue arrows, low expression or negative of Ki67. Red arrows, high expression of Ki67.

693 b. An intraosseous model of bone metastasis was used via direct implantation of NSCLC cells
694 A549 into tibia of nude mice. Three weeks after implantation, mice were sacrificed.
695 Representative immunohistochemical staining of Ki-67 in tibia of tumor-bearing nude mice. The
696 dashed line indicates the boundary between bone and tumor. Scale bars: 50 μm. Blue arrows, low
697 expression or negative of Ki67. Red arrows, high expression of Ki67.

698 c. Schematic diagram of co-culture.

699 d. CCK-8 assays were performed to evaluate the effects of MLO-Y4 cells or MC3T3-E1 cells on
700 the proliferation of A549 cells in the co-culture system. n=6; one-way analysis of variance with
701 Turkey's multiple comparisons test.

702 e. EdU flow cytometry were performed to evaluate the effect of MLO-Y4 cells on the proliferation
703 of A549 cells in the co-culture system.

704 f. CCK-8 assays were performed to evaluate the effect of MLO-Y4 cells on the proliferation of
705 MC3T3-E1 cells in the co-culture system. n=6; Student's two-sided unpaired t test.

706 no significance (ns) $P>0.05$, *$P < 0.05$, **$P < 0.01$, ***$P < 0.001$, ****$P < 0.0001$.

Figure 2

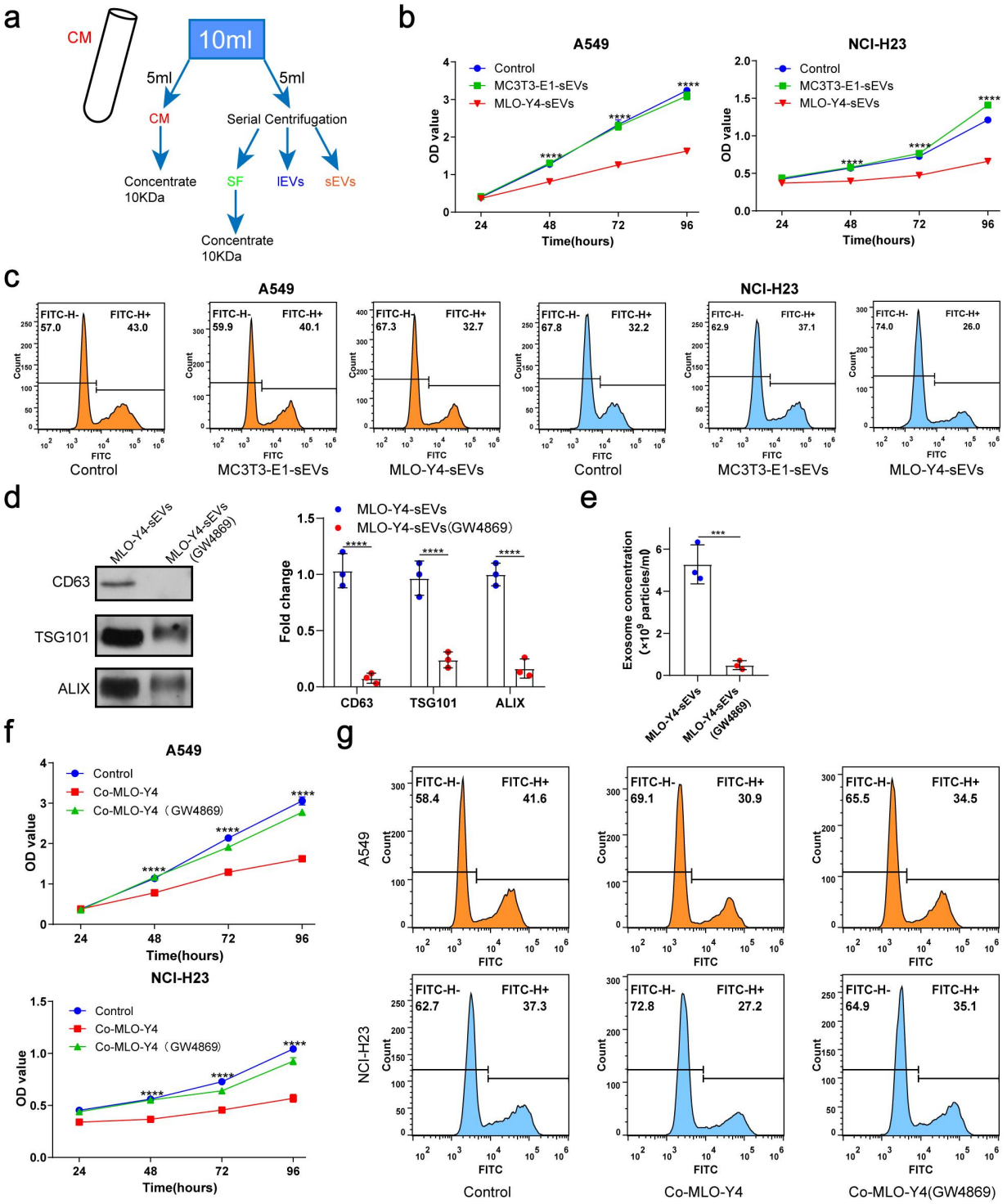
a
CM
10ml
5ml
5ml
CM
Serial Centrifugation
Concentrate 10KDa
SF
lEVs
sEVs
Concentrate 10KDa
b
A549
NCI-H23
Control
MC3T3-E1-sEVs
MLO-Y4-sEVs
OD value
Time(hours)
c
A549
NCI-H23
FITC-H- 57.0
FITC-H+ 43.0
FITC-H- 59.9
FITC-H+ 40.1
FITC-H- 67.3
FITC-H+ 32.7
FITC-H- 67.8
FITC-H+ 32.2
FITC-H- 62.9
FITC-H+ 37.1
FITC-H- 74.0
FITC-H+ 26.0
Count
FITC
Control
MC3T3-E1-sEVs
MLO-Y4-sEVs
Control
MC3T3-E1-sEVs
MLO-Y4-sEVs
d
MLO-Y4-sEVs
MLO-Y4-sEVs (GW4869)
CD63
TSG101
ALIX
MLO-Y4-sEVs
MLO-Y4-sEVs(GW4869)
Fold change
CD63
TSG101
ALIX
e
Exosome concentration (×10^9 particles/ml)
MLO-Y4-sEVs
MLO-Y4-sEVs (GW4869)
f
A549
Control
Co-MLO-Y4
Co-MLO-Y4（GW4869）
OD value
Time(hours)
NCI-H23
Control
Co-MLO-Y4
Co-MLO-Y4（GW4869）
OD value
Time(hours)
g
A549
NCI-H23
FITC-H- 58.4
FITC-H+ 41.6
FITC-H- 69.1
FITC-H+ 30.9
FITC-H- 65.5
FITC-H+ 34.5
FITC-H- 62.7
FITC-H+ 37.3
FITC-H- 72.8
FITC-H+ 27.2
FITC-H- 64.9
FITC-H+ 35.1
Count
FITC
Control
Co-MLO-Y4
Co-MLO-Y4(GW4869)

Figure 2. Osteocyte sEVs inhibited the proliferation of NSCLC cells.

a. Schematic diagram of serial centrifugation and concentration of culture medium. Conditioned medium (CM) was separated into soluble factor (SF), large extracellular vesicles (lEVs), and small extracellular vesicles (sEVs) fractions, by serial ultracentrifugation and ultrafiltration.

b. CCK-8 assays were performed to evaluate the effect of sEVs on the proliferation of NSCLC cells. n=4, two-way analysis of variance with Sidak's multiple comparisons test.

c. EdU flow cytometry were performed to evaluate the effect of sEVs on the proliferation of NSCLC cells.

d. Western blot analysis of the typical sEVs markers CD63, TSG101, and Alix. n=3; Student's two-sided unpaired t test.

e. The concentration of the sEVs were detected by NanoSight Analysis. n=3; Student's two-sided unpaired t test.

f. CCK-8 assays were performed to evaluate the rescue effect of GW4869 on the proliferation of NSCLC cells co-cultured with MLO-Y4 cells. n=4, two-way analysis of variance with Sidak's multiple comparisons test.

g. EdU flow cytometry were performed to evaluate the rescue effect of GW4869 on the proliferation of NSCLC cells co-cultured with MLO-Y4 cells.

no significance(ns) $P>0.05$, *$P < 0.05$, **$P < 0.01$, ***$P < 0.001$, ****$P < 0.0001$.

Figure 3

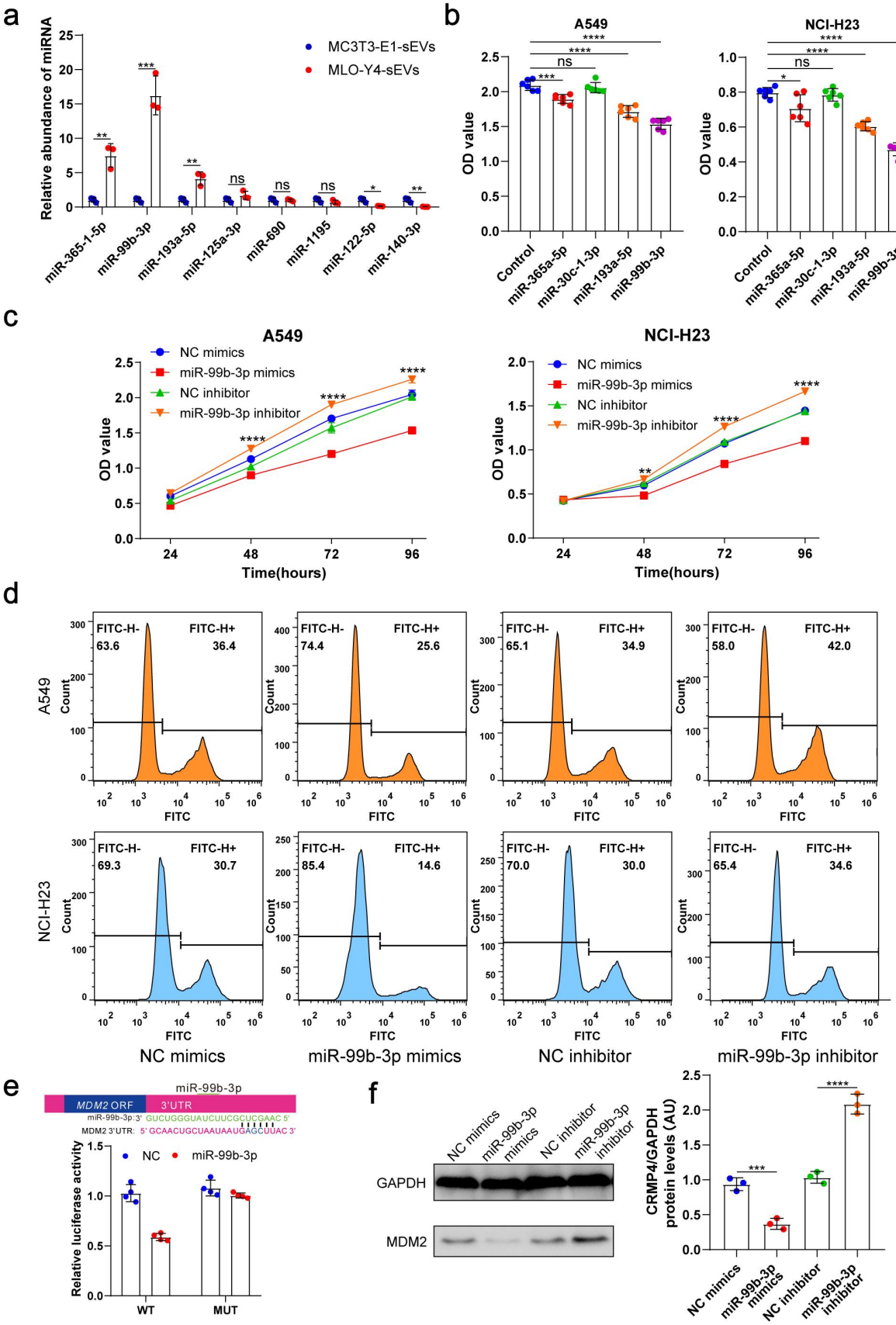
a
Relative abundance of miRNA
MC3T3-E1-sEVs
MLO-Y4-sEVs
miR-365-1-5p
miR-99b-3p
miR-193a-5p
miR-125a-3p
miR-690
miR-1195
miR-122-5p
miR-140-3p
b
A549
NCI-H23
OD value
Control
miR-365a-5p
miR-30c-1-3p
miR-193a-5p
miR-99b-3p
c
A549
NCI-H23
NC mimics
miR-99b-3p mimics
NC inhibitor
miR-99b-3p inhibitor
OD value
Time(hours)
d
A549
NCI-H23
Count
FITC
FITC-H-
FITC-H+
63.6
36.4
74.4
25.6
65.1
34.9
58.0
42.0
69.3
30.7
85.4
14.6
70.0
30.0
65.4
34.6
NC mimics
miR-99b-3p mimics
NC inhibitor
miR-99b-3p inhibitor
e
miR-99b-3p
MDM2 ORF
3'UTR
miR-99b-3p:3' GUCUGGGUAUCUUCGCUCGAAC 5'
MDM2 3'UTR: 5' GCAACUGCUAAUAAUGAGCUUAC 3'
Relative luciferase activity
NC
miR-99b-3p
WT
MUT
f
NC mimics
miR-99b-3p mimics
NC inhibitor
miR-99b-3p inhibitor
GAPDH
MDM2
CRMP4/GAPDH protein levels (AU)

730 **Figure 3. Osteocyte sEVs miR-99b-3p inhibited the proliferation of NSCLC cells by directly**

731 **targeting MDM2.**

732 a. Comparison of relative miR-365-1-5p, miR-99b-3p, miR-193a-5p, miR-125a-3p, miR-690,

733 miR-1195, miR-122-5p, miR-140-3p content between MLO-Y4-sEVs and MC3T3-E1-sEVs by

734 qRT-PCR. n=3, student's two-sided unpaired t test.

735 b. NSCLC cells were transfected with miR-365a-5p, miR-30c-1-3p, miR-193a-5p, miR-99b-3p

736 mimics, or NC (negative control) in DMEM medium. 48 hours later, CCK-8 assays were

737 performed. n=6, one-way analysis of variance with Turkey's multiple comparisons test.

738 c, d. NSCLC cells were transfected with miR-99b-3p mimics, NC mimics, miR-99b-3p inhibitor

739 and NC inhibitor. 48 hours later, EdU flow cytometry were performed. CCK-8 assays were

740 performed at different points in time after transfection. n=6, two-way analysis of variance with

741 Sidak's multiple comparisons test.

742 e. Schematic diagram of putative miR-99b-3p binding sites in the MDM2 3′-UTR. Green letters

743 denote mutation sites. Relative luciferase activities of wild-type (WT) or mutant (MUT) MDM2

744 3′-UTRs were determined in A549 cells, which were co-transfected with the miR-99b-3p mimics

745 or negative control. Luciferase activity was normalized using Renilla. n=4, Student's two-sided

746 unpaired t test.

747 f. MDM2 protein in A549 cells were analyzed by Western blot 72 hours after transfection. n=3;

748 one-way analysis of variance with Turkey's multiple comparisons test.

749 no significance(ns) $P>0.05$, *$P < 0.05$, **$P < 0.01$, ***$P < 0.001$, ****$P < 0.0001$.

Figure 4

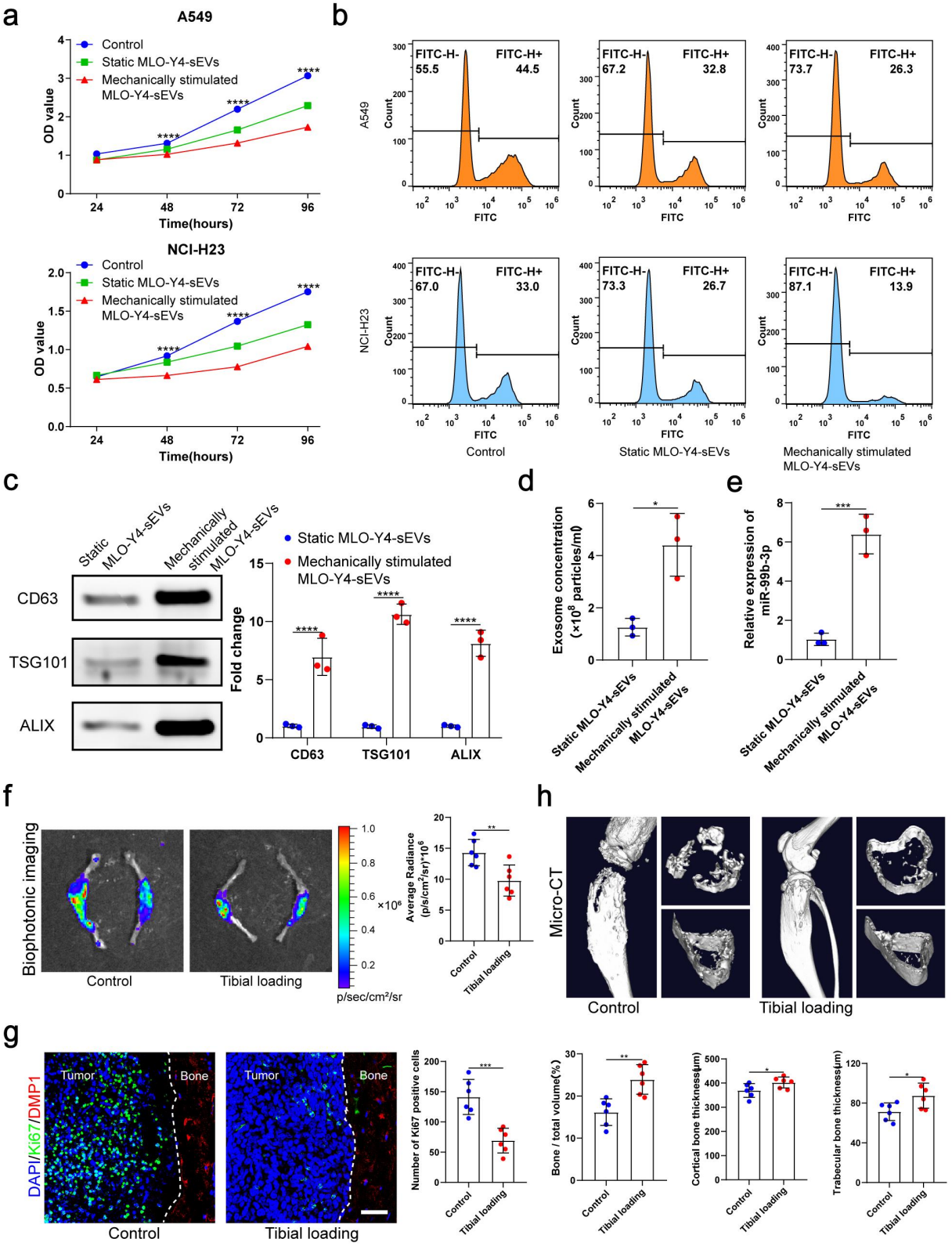
a
A549
Control
Static MLO-Y4-sEVs
Mechanically stimulated MLO-Y4-sEVs
OD value
Time(hours)
NCI-H23
b
A549
NCI-H23
FITC-H-
FITC-H+
Count
FITC
Control
Static MLO-Y4-sEVs
Mechanically stimulated MLO-Y4-sEVs
c
Static MLO-Y4-sEVs
Mechanically stimulated MLO-Y4-sEVs
CD63
TSG101
ALIX
Fold change
d
Exosome concentration (×10^8 particles/ml)
e
Relative expression of miR-99b-3p
f
Biophotonic imaging
Control
Tibial loading
p/sec/cm²/sr
Average Radiance (p/s/cm²/sr)*10^6
h
Micro-CT
g
DAPI/Ki67/DMP1
Tumor
Bone
Number of Ki67 positive cells
Bone / total volume(%)
Cortical bone thickness(μm)
Trabecular bone thickness(μm)

752 **Figure 4. Mechanical stimulation increased the release of sEVs from osteocytes and**

753 **enhanced inhibitory effect of osteocytes on the proliferation of NSCLC cells.**

754 a. MLO-Y4 cells were mechanically stimulated by stretching at 12% strain at a 1.25 Hz frequency

755 for 12 h, and sEVs were extracted from the conditioned medium. CCK-8 assays were performed

756 to evaluate the effect of sEVs on the proliferation of NSCLC cells. n=4, two-way analysis of

757 variance with Sidak's multiple comparisons test.

758 b. EdU flow cytometry were performed to evaluate the effect of sEVs on the proliferation of

759 NSCLC cells.

760 c. Western blot analysis of the typical sEVs markers CD63, TSG101, and Alix. n=3, student's

761 two-sided unpaired t test.

762 d. Concentration of sEVs was detected by NanoSight analysis. n=3, student's two-sided unpaired t

763 test.

764 e. Mechanical loading was applied to the tibiae with bone metastasis via direct implantation of

765 GFP-LLC into tibia of mouse. qRT-PCR identification of miR-99b-3p in sEVs. n=3, student's

766 two-sided unpaired t test.

767 f. Representative biophotonic images and quantification of fluorescence signal in hindlimb bones

768 of mice. n=6, student's two-sided unpaired t test.

769 g. Representative immunofluorescence staining images of Ki-67(green), DMP1(red), and DAPI

770 (blue) in the tibia of mice with bone metastases and quantification of the number of Ki-67-positive

771 cells in the images. The dashed line indicates the boundary between bone and tumor. Scale bars:

772 50 μm. n=6, student's two-sided unpaired t test.

773 h. Representative micro-CT imaging and quantitation of the tibia (bone/total volume, cortical bone

774 thickness, trabecular bone thickness) in mice. n=6, student's two-sided unpaired t test.

775 no significance(ns) P>0.05, *P < 0.05, **P < 0.01, ***P < 0.001, ****P < 0.0001.

776

Figure 5

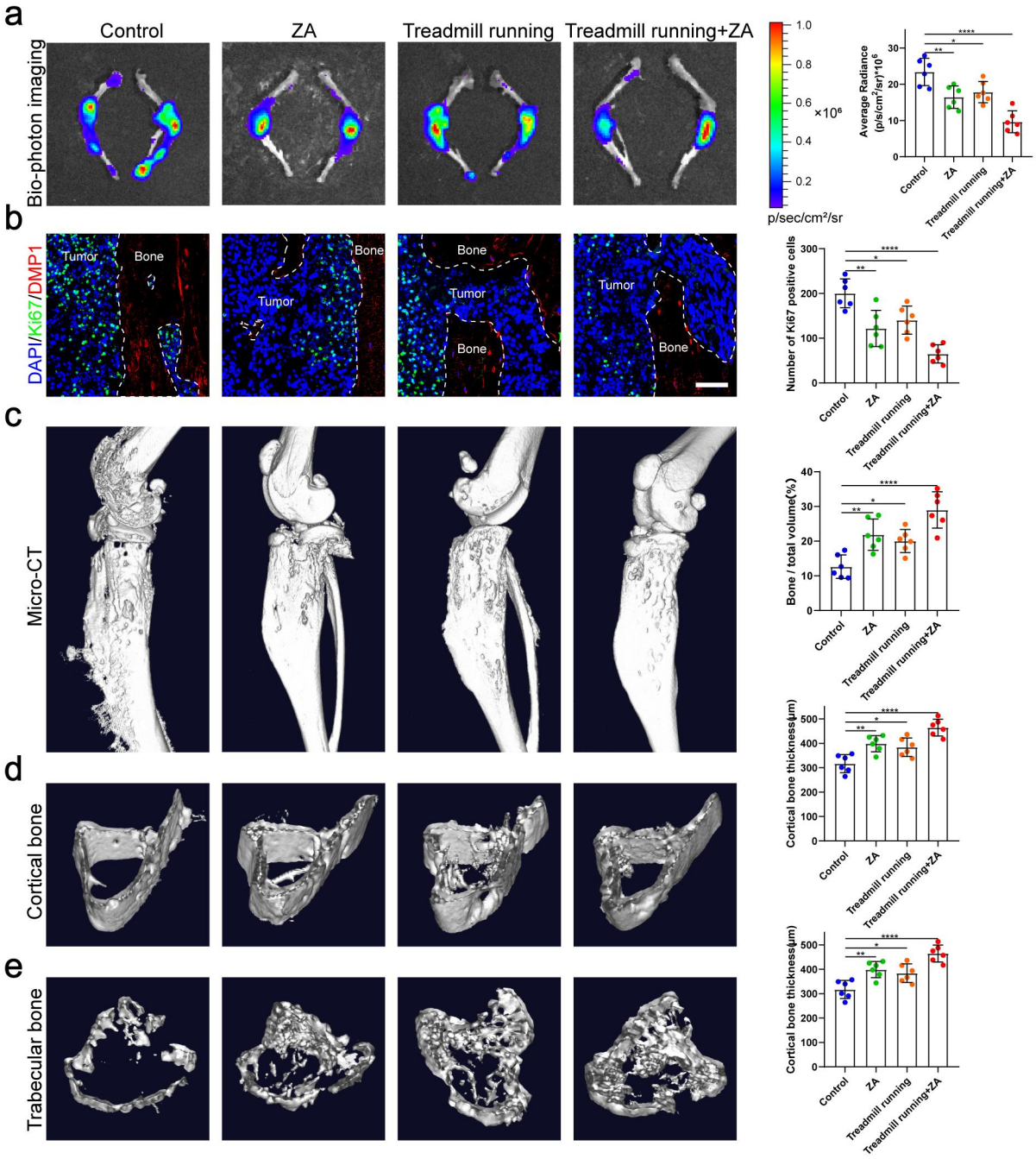
a
Control
ZA
Treadmill running
Treadmill running+ZA
Bio-photon imaging
1.0
0.8
0.6
0.4
0.2
×10⁶
p/sec/cm²/sr
Average Radiance (p/s/cm²/sr)*10⁶
b
DAPI/Ki67/DMP1
Tumor
Bone
Number of Ki67 positive cells
c
Micro-CT
Bone / total volume(%)
d
Cortical bone
Cortical bone thickness(μm)
e
Trabecular bone
Cortical bone thickness(μm)
Control
ZA
Treadmill running
Treadmill running+ZA

779 **Figure 5. Moderate exercise combined with zoledronic acid effectively suppressed the**

780 **progression of bone metastasis of NSCLC.**

781 An intraosseous model of bone metastasis was used via direct implantation of murine Lewis lung

782 carcinoma (LLC) cells expressing green fluorescent protein (GFP) into tibia of mouse. Mice were

783 subsequently randomized into tumor-bearing only (control), zoledronic acid (ZA), treadmill

784 running, and treadmill running combined zoledronic acid (treadmill running+ZA) groups. Four

785 weeks later, mice were sacrificed.

786 a. Representative biophotonic images and quantification of fluorescence signal in hindlimb bones

787 of mice. n=6, one-way analysis of variance with Turkey's multiple comparisons test.

788 b. Representative immunofluorescence staining images of Ki-67(green), DMP1(red), and DAPI

789 (blue) in the tibia of mice with bone metastases and quantification of the number of Ki-67-positive

790 cells in the images. The dashed line indicates the boundary between bone and tumor. Scale bars:

791 50 μm. n=6, one-way analysis of variance with Turkey's multiple comparisons test.

792 c-e Representative micro-CT imaging and quantitation of the tibia (bone/total volume, cortical

793 bone thickness, trabecular bone thickness) in mice. n=6, one-way analysis of variance with

794 Turkey's multiple comparisons test.

795 no significance (ns) $P>0.05$, *$P < 0.05$, **$P < 0.01$, ***$P < 0.001$, ****$P < 0.0001$.

Figure 6

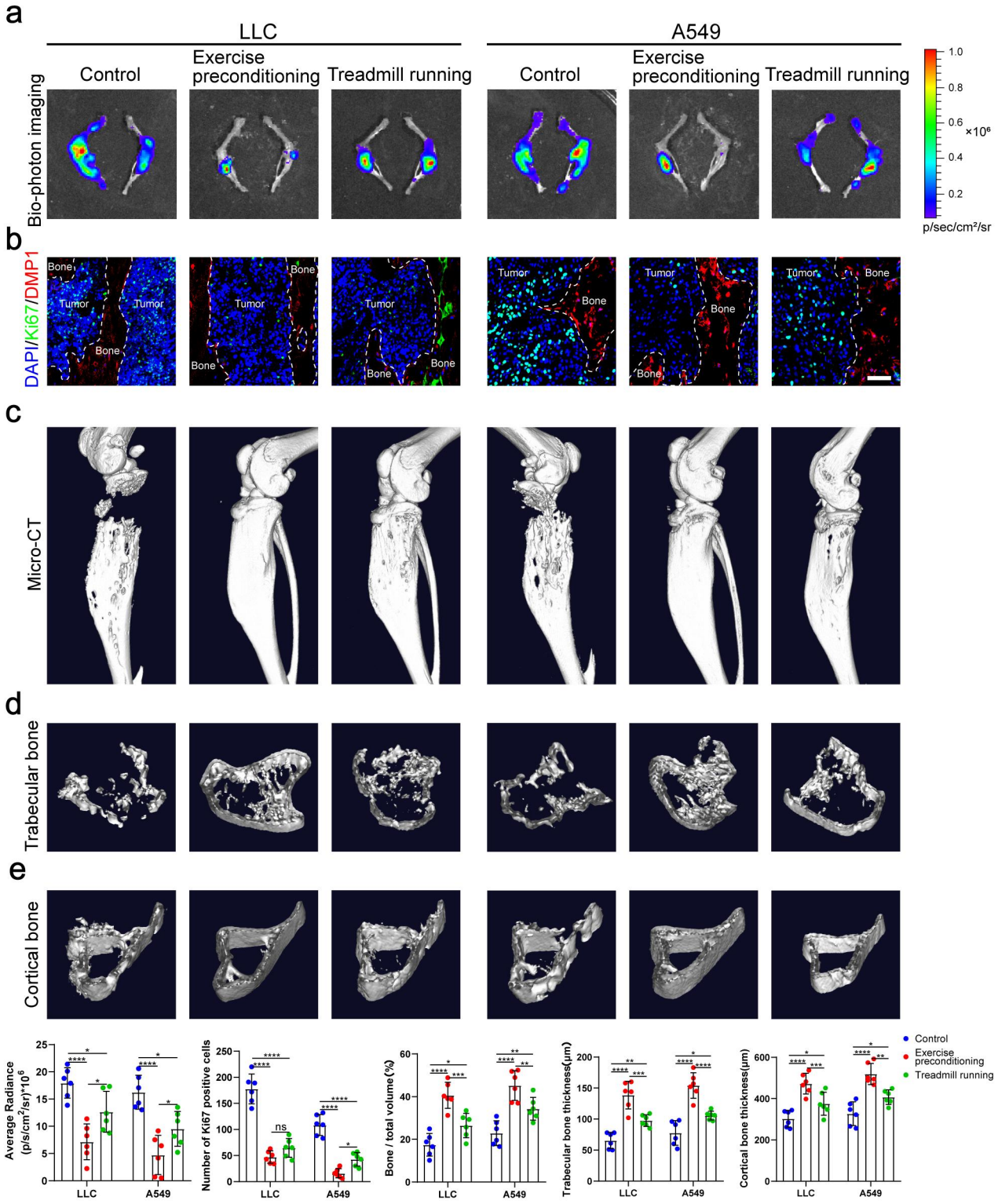
a
LLC
A549
Control
Exercise preconditioning
Treadmill running
Control
Exercise preconditioning
Treadmill running
Bio-photon imaging
1.0
0.8
0.6
×10⁶
0.4
0.2
p/sec/cm²/sr
b
DAPI/Ki67/DMP1
Bone
Tumor
c
Micro-CT
d
Trabecular bone
e
Cortical bone
Average Radiance (p/s/cm²/sr)*10⁶
Number of Ki67 positive cells
Bone / total volume (%)
Trabecular bone thickness(μm)
Cortical bone thickness(μm)
LLC
A549
ns
Control
Exercise preconditioning
Treadmill running

798 **Figure 6. Exercise preconditioning effectively suppressed the progression of bone metastasis**

799 **of NSCLC.**

800 An intraosseous model of bone metastasis was used via direct implantation of NSCLC cells (LLC

801 and A549) into tibia of mouse. Mice were subsequently randomized into tumor-bearing only

802 (control), treadmill running before and after implantation of NSCLC cells into tibia (exercise

803 preconditioning), and treadmill running after implantation of NSCLC cells into tibia (treadmill

804 running) groups. For exercise preconditioning group, mice were subjected to 4 weeks of treadmill

805 exercise before implantation of NSCLC cells into tibia of mouse. Four weeks after implantation,

806 mice were sacrificed.

807 a. Representative biophotonic images and quantification of fluorescence signal in hindlimb bones

808 of mice. n=6, one-way analysis of variance with Turkey's multiple comparisons test.

809 b. Representative immunofluorescence staining images of Ki-67(green), DMP1(red), and

810 DAPI(blue) in the tibia of mice with bone metastases and quantification of the number of

811 Ki-67-positive cells in the images. The dashed line indicates the boundary between bone and

812 tumor. Scale bars: 50 μm. n=6, one-way analysis of variance with Turkey's multiple comparisons

813 test.

814 c-e Representative micro-CT imaging and quantitation of the tibia (bone/total volume, cortical

815 bone thickness, trabecular bone thickness) in mice. n=6, one-way analysis of variance with

816 Turkey's multiple comparisons test.

817 no significance (ns) $P>0.05$, *$P < 0.05$, **$P < 0.01$, ***$P < 0.001$, ****$P < 0.0001$.

818 **Figure 7**

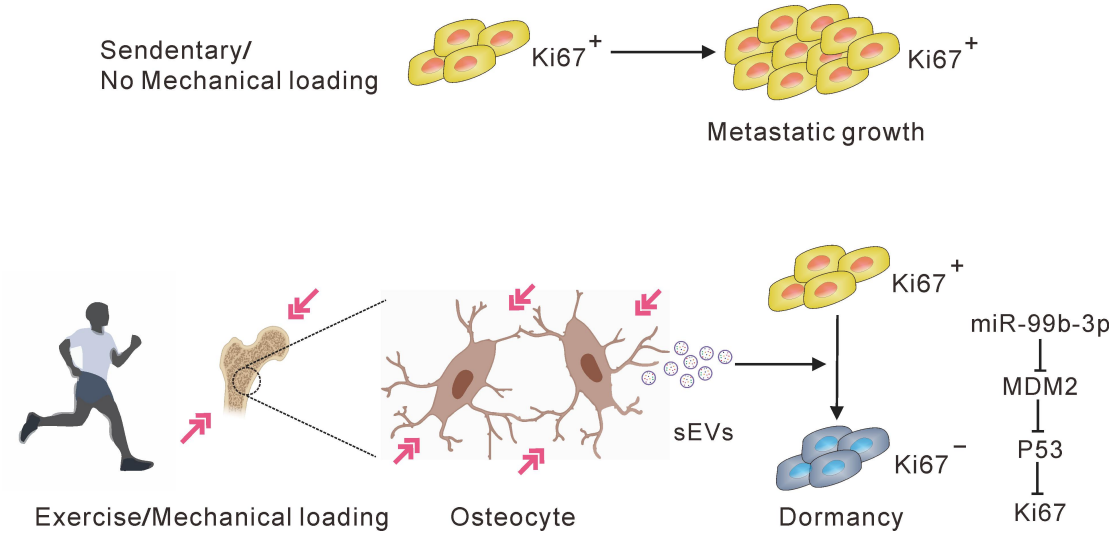

819

820

821 **Figure 7. A hypothetic model depicting osteocytes induce and maintain tumor dormancy in**

822 **bone metastasis of non-small cell lung cancer.**

823 Osteocytes, sensing mechanical stimulation generated by exercise or mechanical loading, inhibit

824 the proliferation and sustain the dormancy of NSCLC cells by releasing sEVs with tumor

825 suppressor miRNAs, such as miR-99b-3p, which inhibits the proliferation of NSCLC cells by

826 directly targeting MDM2.